

Velocity dependence of electron-capture partial cross sections and alignment in low-energy collisions of Ne^{8+} and Ar^{8+} with atomic Na

David M. Gauntt* and Karsten Danzmann†

Department of Physics, Stanford University, Stanford, California 94305

(Received 8 April 1991; revised manuscript received 28 April 1992)

We have measured the intensities and polarizations of fine-structure lines in the $N=9-8$ manifolds of Ne VIII and Ar VIII spectra produced in collisions of Ne^{8+} and Ar^{8+} ($v=0.05-0.15$ a.u.) with atomic sodium, and determined alignment and partial cross sections for electron capture as functions of projectile velocity. At low velocity the partial cross section for capture into the S levels is significantly higher than for capture into higher L levels, and at higher velocities the higher- L partial cross sections increase for Ar VIII and dominate for Ne VIII. The low- L -level cross sections are in fair agreement with multichannel-Landau-Zener calculations, while the high- L -level cross sections are in qualitative disagreement. For the neon projectiles, the polarization of the Bohr line is approximately 0.3 and independent of velocity; for argon projectiles, the polarization is approximately 0.15 and increases with increasing velocity. A qualitative theoretical interpretation is offered.

PACS number(s): 34.70.+e, 32.30.Jc

I. INTRODUCTION

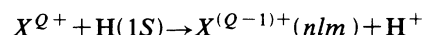
The development of sources of highly charged, low-energy ions has increased interest in the collisions of atoms and ions at low velocities; that is, at internuclear velocities lower than the orbital velocity of the valence electrons of the collision partners. These collisions are of fundamental theoretical interest as tests of time-dependent few-body quantum mechanics, and of practical interest as processes seen in astrophysical plasmas and controlled fusion plasmas. In particular, electron capture is a process that is believed to contribute greatly to cooling in thermonuclear plasmas. The theory of electron capture in low-velocity collisions has progressed from order-of-magnitude calculations of total cross sections to predictions of partial cross sections and subshell alignments.

A. Theoretical development

The process of electron capture may be divided into primary and secondary interactions. Primary-capture interactions are those between states that correspond at large internuclear separation to states centered about different ions, and secondary interactions are those between states centered about the same ion, usually the projectile. Early calculations [1] predicted statistical populations of the orbital-angular-momentum subshells. These early attempts to calculate partial-capture cross sections dealt only with primary-capture interactions and failed to take into account interactions between states of the projectile after the collision, interactions which can be thought of as Stark mixing of the atomic states induced by the electric field of the target. Salin [2] has calculated partial cross sections for capture from atomic hydrogen onto fully stripped targets taking the Stark interactions into account; he found that capture is predominantly into the $M=0$ and ± 1 (σ and π) states, and that the popula-

tion of each M manifold is mixed among the angular momentum subshells in the manifold ("complete mixing model"), so that the populations of the subshells are nearly equal but with a slight deficiency in the S subshell. However, because of the degeneracy of the final states of the projectile, experimental studies of such systems using either energy-loss or optical techniques are not practical.

Harel and Jouin [3], using a close-coupling model, calculated partial cross sections for the electron-capture process



for the projectiles $X=\text{O}$, Ne , and Ar . They found that for constant projectile charge Q , at low velocities ($v_{\text{proj}} < 0.3$ a.u.) increasing the atomic number of the projectile increases the cross section of capture into S levels and decreases the cross section of higher L levels; the dependence of the L distribution on the atomic number disappears at higher velocities. Harel and Salin [4] have calculated the polarization of light emitted in $P-S$ transitions from the M distributions of Harel and Jouin's calculations, and predict the polarization to increase as velocity increases from $v=0.2$ to 0.8 a.u., implying an increase in the population of final σ states. At high velocity they found the polarization to be independent of the atomic number of the projectile, and at low velocity the influence of the atomic number on the polarization is greater for the many-electron system ($\text{Ar}^{8+} + \text{H}$) than for the few-electron systems ($\text{O}^9 + \text{H}$, $\text{Ne}^{8+} + \text{H}$).

B. Experimental development

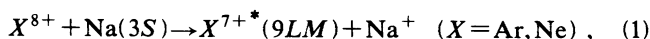
Experimental work on electron capture has concentrated on two techniques; energy-loss spectroscopy and photon spectroscopy. The former technique is useful in determining total, N , and L cross sections with high efficiency but has an energy resolution on the order of 10% and is not sensitive to variations in the M distribu-

tion of the final states [5]. Photon spectroscopy has higher resolution and the ability through polarization measurements to measure the degree of alignment of M states, but has much lower detection efficiency [6]. Experiments using both techniques often are performed using electron cyclotron resonance (ECR) [7] or electron beam ion source (EBIS) [8] ion sources which produce beams of high temperature; the resulting Doppler spread of the emitted photons places an ultimate limit on the resolution of the measurements. Also, since the target is usually a tightly bound system such as helium or either atomic or molecular hydrogen, capture takes place into low-lying states from which the only electromagnetic decay transitions are in the x-ray or vuv range; this requires the use of low-sensitivity spectrometers and detectors. Few polarization measurements have been published, so little is known of the M distributions of the final states. The use of recoil ion sources [9] to produce well-collimated low-temperature beams and visible light spectroscopy to improve the energy resolution of the experiment addresses the drawbacks of vuv high-temperature spectroscopy.

The requirement that the spectrum of the projectile after capture contain lines in the visible range demands that the electron be captured into relatively high-lying states [10]. In turn, according to the classical barrier model (see below) this demands the use of a target with a low ionization energy. The best candidates are the alkali-metal and some rare-earth elements. Of these it is easiest and safest to produce an atomic beam of sodium, potassium, or cesium. The choice of projectile is dictated by the physics of the recoil ion beam source. Polyatomic molecules produce very weak beams; this is believed to be due to the Coulomb repulsion that results when most of the electrons of the molecule are stripped away. This heats the recoil plasma and reduces the efficiency of the recoil ion source which is designed with a small phase-space acceptance. Therefore, the best projectile candidates are the noble gases; of these, helium, neon, and argon are the most readily obtainable.

Lembo *et al.* [11] have measured optical emission cross sections and polarizations for light emitted by the high- L subshells of Ne^{q+} recoil ions following electron capture from atomic sodium. They found evidence that for ions with two or fewer core electrons, capture into the high- L subshells is predominantly into the σ states, in accord with Salin's "complete mixing" model, but that adding electrons to the core decreases the population of the higher- L subshells as well as decreasing the alignment of these levels. Comparing these measurements to previous measurements of the total capture cross section they inferred that increasing the number of electrons in the core also increases the final population of the lower- L subshells.

We have observed light emitted after the collision process



using a low-velocity recoil ion beam and a spectrometer polarimeter. We chose the $8+$ projectile charge states since these have emission lines in the blue where our pho-

tomultiplier tube (PMT) efficiency is high, and the projectile cores have zero angular momentum and simple spectra. Capture in these systems is primarily into the $N=9$ shell according to the classical barrier model [12], and into the $N=8$ shell according to the modified multichannel Landau-Zener model of Taulbjerg [13]. We were able to measure the polarization of the $N=9 \rightarrow 8$ Bohr line ($L_{\text{init}} > 6$) for both Ne VIII and Ar VIII, and of the $9P-8D$ and $9D-8F$ of the Ar VIII spectrum, as functions of velocity, and the intensities of these lines as well as the $9S-8P$ lines of both systems. From the intensities of fine-structure lines we were able to determine partial cross sections for capture into the $N=9$ shell.

C. Notation and nomenclature for molecular orbitals and molecular states

Since we are studying systems in which the projectile and target ions are alkali-metal- or hydrogenlike and have cores with no spin or orbital angular momentum, we label the molecular states (or exit channels) by the orbital of the active electron. Following Herzberg [14], the σ orbital corresponding in the separated-atom limit to the $1s$ orbital about ion A is labeled as $\sigma 1s_A$, so the molecular state is $\Sigma 1S_A$; to simplify the notation the charge is left off the ion designation A . Thus, the lowest-energy Σ and Π states of $(\text{NeNa})^{8+}$ corresponding to the $N=9$ manifold of Ne^{7+} are $\Sigma 9S_{\text{Ne}}$ and $\Pi 9P_{\text{Ne}}$. Labeling hydrogenlike systems is trickier since in nonrelativistic quantum mechanics the molecular orbitals correspond at infinity to parabolic, rather than spherical, states. To remain consistent with the labeling of the alkalilike ion we label the $N=9\Sigma$ states of O^{7+} in order of increasing energy as $\Sigma 9S_{\text{O}}$, $\Sigma 9P_{\text{O}}$, etc., and the Π states as $\Pi 9P_{\text{O}}$, $\Pi 9D_{\text{O}}$, etc. The entrance channel is labeled as though there were no coupling at pseudocrossings between entrance and exit channels; i.e., $\Sigma 3S_{\text{Na}}$.

We use the name "shell" for all states that correspond in the separated-atom (SA) limit to states with a given N , and "subshell" for the manifold of all states that correspond to states with a given L ; we will label molecular subshells with an " L " index in analogy with the quantum number L that labels an atomic subshell, although in diatomic molecules the orbital angular momentum is not a constant of the motion. The terms "state" and "level" are used interchangeably in molecular systems, since states are at most doubly degenerate in most cases.

II. THEORY

A. The classical barrier model

The simplest theory used in describing electron capture is the classical barrier model [15] (CBM), a semiclassical model that has been shown to predict total capture cross sections [16] to within a factor of 2, but does not provide information on L or M distributions or velocity dependencies. The theory predicts that capture is highly selective, with only one or two shells populated.

B. The multichannel Landau-Zener model

The multichannel Landau-Zener (MLZ) model provides information on velocity and L dependence of cross

sections. Salop and Olson [17] have proposed a form for the interaction matrix element for partially stripped projectiles and targets for use in a simple absorbing sphere model (ASM), a variation of the CBM. The ASM assumes that many crossings are available for the primary capture. Taulbjerg [13] has proposed a modification of Salop and Olson's matrix elements that allows calculation of L distributions in partially stripped projectiles in a multichannel Landau-Zener model (MLZ); however, because this treatment assumes a significant capture probability into only one level at a time, Taulbjerg states that the crossings of the subshells must be well separated for his treatment. Several studies have confirmed the accuracy of this approach [13,18]. We have attempted to extend Taulbjerg's MLZ model to a many-crossing system by using the multichannel approach of Kimura *et al.* [19], with the matrix elements between entrance and exit channels

$$H_{12} = AH_{KT} \quad (2)$$

where

$$H_{KT} = \frac{9.13f_{n1}}{\sqrt{q}} \exp \left[-\frac{1.324R_c\alpha}{\sqrt{q}} \right]$$

is Taulbjerg's matrix element, and A is a scaling parameter that we adjusted to fit the model to the experimental data. Both the absorbing sphere model (ASM) and MLZ model deal with primary-capture processes, but like the CBM neither the ASM nor the MLZ model accounts for secondary interactions.

C. Close-coupling models

The most accurate electron-capture models are generated by using the one-electron time-dependent Schrödinger equation with an electrostatic potential defined by the nuclei of the ions and the core electrons [20]. When the wave function of the active electron is expanded in terms of an arbitrary orthonormal basis set using the internuclear axis as the axis of quantization

$$|\psi(t, R)\rangle = \sum_i a_i(t) e^{-i\omega_i t} |\Phi_i(R)\rangle, \quad (3)$$

where R is the internuclear distance, and the projectile is assumed to follow a linear trajectory parametrized by the distance $x = vt$, then the time-dependent Schrödinger equation leads to the linear system of equations

$$i \frac{\partial}{\partial x} a_k = [M^{\text{pot}}(v, R) + M^{\text{rad}}(b, R) + M^{\text{rot}}(b, R)]_{nk} \times a_n \exp \left[-i \left[\frac{\omega_k - \omega_n}{v} \right] x \right], \quad (4)$$

where

$$M_{nk}^{\text{pot}} \equiv \frac{1}{v} \langle \Phi_n | V_{\text{core}} | \Phi_k \rangle$$

is the potential interaction matrix,

$$M_{nk}^{\text{rad}} \equiv -i \frac{b}{R} \left\langle \Phi_n \left| \frac{\partial}{\partial R} \right| \Phi_k \right\rangle$$

is the radial interaction matrix,

$$M_{nk}^{\text{rot}} \equiv -\frac{b}{R^2} \langle \Phi_n | L_y | \Phi_k \rangle$$

is the rotational interaction matrix, V_{core} is the electrostatic potential of any core electrons not included in the Hamiltonian used to generate the basis set $|\Phi_n\rangle$, v is the projectile speed, R is the internuclear axis, and L_y is the y component of the angular momentum operator.

In this parametrization of Schrödinger's equation the velocity enters only in the denominator of the core coupling matrix element and in the exponential factor. The radial and rotational couplings are weakened when the factor $(\omega_k - \omega_n)/v$ in the exponent is large; this is the case for small velocities or large energy splittings. The interaction matrix elements have been separated into purely geometric terms times reduced interaction matrices $\langle \Phi_n | (\partial/\partial R) | \Phi_k \rangle$ and $\langle \Phi_n | L_y | \Phi_k \rangle$. As the internuclear separation approaches infinity, the internuclear axis approaches the velocity axis of the projectile, and the states $|\Phi_n\rangle$ should be chosen to converge to atomic orbital wave functions quantized along the projectile velocity axis. In the case of hydrogenic systems the exit channels converge to Stark wave functions, and special care must be taken in interpreting the results [2]. If the states $|\Phi_n\rangle$ are adiabatic molecular orbitals (MO), or the eigenstates of the total electrostatic potential, then $V_{\text{core}} = 0$ and the only interactions are the radial and rotational interactions. The symmetry of multielectron systems is determined by the quantum number Λ , the component of total orbital angular momentum along the internuclear axis [21]. Radial interactions generate transitions between basis states of similar symmetry at pseudocrossings of the system energy levels and are caused by the inability of the electron cloud to conform to basis states changing rapidly in shape; rotational interactions generate transitions between basis states of adjacent values of Λ and are caused by the inability of the electron cloud to rotate with the internuclear axis. States of a given Λ converge at infinity to atomic states of a given M_L ; since the M_L distribution of the final states determines the polarization of the emitted light and the rotational couplings determine the population of the Λ states, the polarization of emitted light can provide information about the rotational coupling. If the states $|\Phi_n\rangle$ are one-electron diatomic molecule orbitals (OEDM), or the eigenstates of a pure one-electron system with nuclear charges set equal to the net charges of the ions, then for nonhydrogenic systems $V_{\text{core}} \neq 0$ and a new set of interactions, the potential couplings, are active. However, at high velocity the potential couplings are less important [4], and the model predictions of cross section and polarization become independent of the core structure.

D. The Stark interaction model

Energy-level diagrams of the adiabatic Σ states of the systems $(\text{OH})^{8+}$, $(\text{NeNa})^{8+}$, and $(\text{ArNa})^{8+}$ are presented in Figs. 1–3, and the rotational interactions near the crossing radius are presented schematically in Figs. 4–6. The projectile energy levels are of molecular orbitals calculated using the Stark approximation; in this approxi-

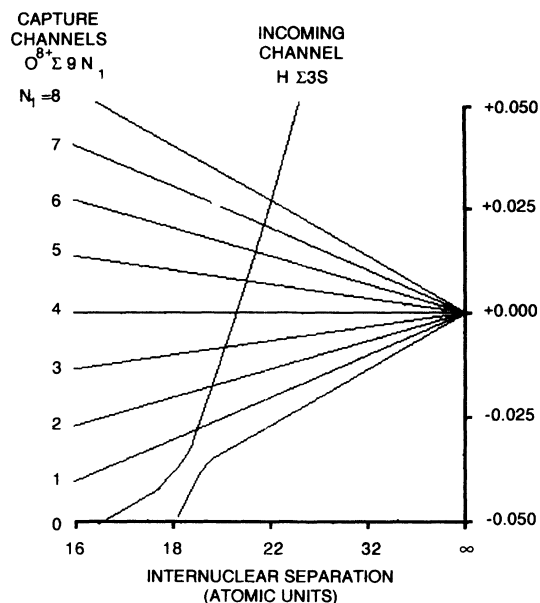


FIG. 1. Energy-level diagram for $(\text{OH})^{8+}$ adiabatic molecular orbitals. The distance scale is linear in R^{-2} , and is proportional to the electric field strength at the projectile. The Coulomb repulsion of the ions after capture has been subtracted from the energies. Only Σ states are plotted; for other states see Fig. 4.

mation the basis states are eigenstates of the Stark Hamiltonian, which approximates the potential couplings between atomic orbitals of the projectile as a Stark interaction caused by the electric field of the target:

$$\mathbf{H}_{ij} = H_{ii}\delta_{ij} - E_z \mathbf{P}_{ij}, \quad (5)$$

where H_{ii} is the separated-atom energy of the projectile, E_z is the strength along the internuclear axis of the elec-

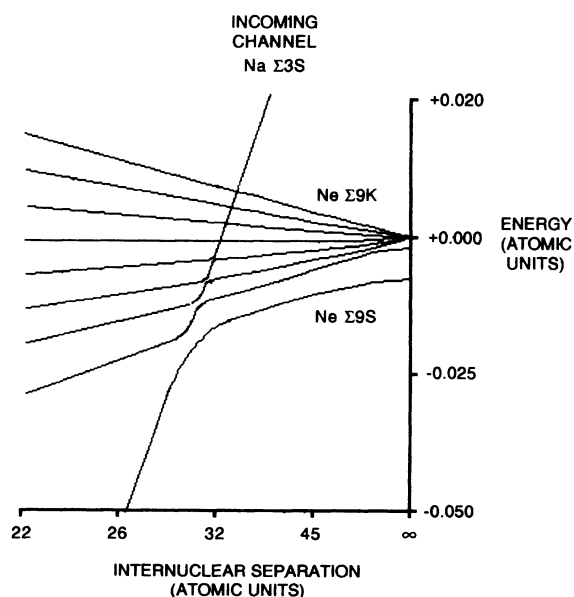


FIG. 2. Energy-level diagram for $(\text{NeNa})^{8+}$ adiabatic molecular orbitals; see caption to Fig. 1.

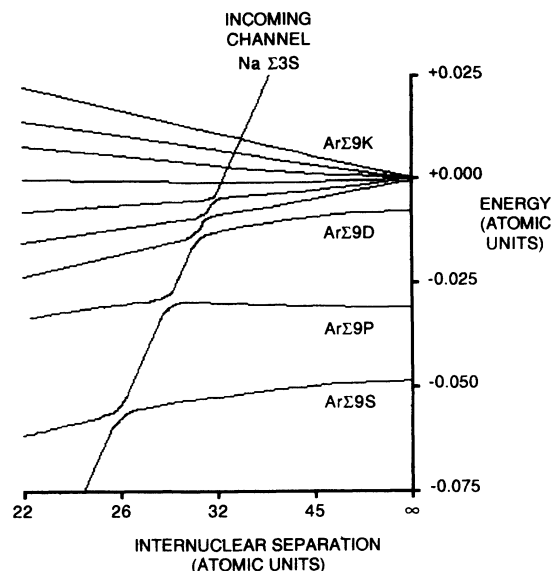


FIG. 3. Energy-level diagram for $(\text{ArNa})^{8+}$ adiabatic molecular orbitals; see caption to Fig. 1.

tric field of the target core at the position of the projectile, and \mathbf{P}_{ij} is the dipole matrix element between projectile atomic states i and j .

The Coulomb repulsion of the nuclei and the Coulomb energy of the electron in the target well have been subtracted. The Stark model breaks down when the target and projectile states interact, and so is quantitatively useful only for interactions at internuclear separations large compared to the crossing radius. At large internuclear separation the eigenvectors of this Hamiltonian are the molecular orbitals of the projectile, and the eigenvalues

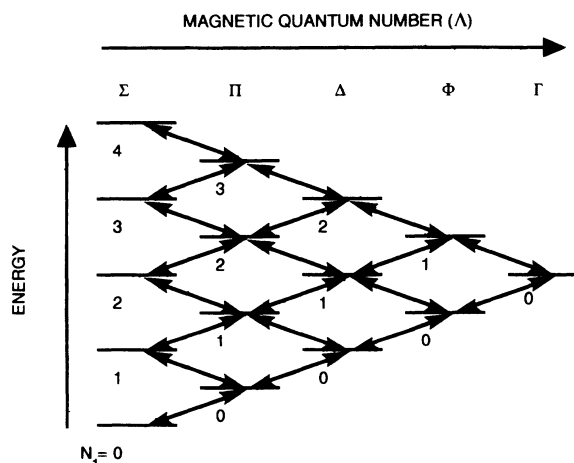


FIG. 4. Schematic diagram of rotational coupling near the crossing radius in the system $(\text{OH})^{8+}$; not all $N=9$ levels are shown. The vertical axis indicates the energy of each state, and the arrows indicate allowed couplings; the strengths of the couplings are about equal. The parameter N_1 is a quantum number of the Stark state, and Λ is the projection of the orbital angular momentum along the internuclear axis, which corresponds to M in spherical bases.

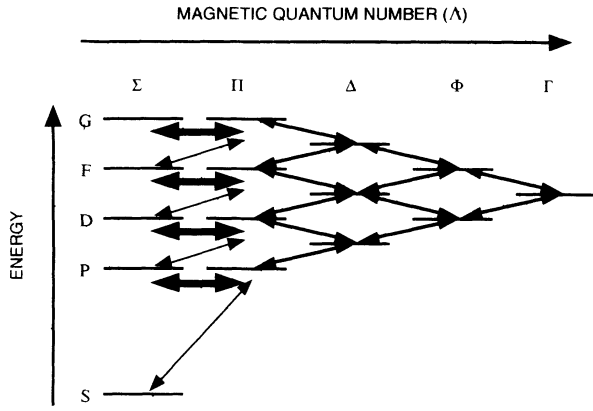


FIG. 5. Schematic diagram of rotational coupling near the crossing radius in the system $(\text{NeNa})^{8+}$; not all $N=9$ levels are shown. The weight of each arrow indicates the strength of the coupling.

are the MO energy levels. They converge asymptotically in the separated-atom (SA) limit (infinite internuclear radius) to the atomic-orbital (AO) wave functions. We calculated the atomic-orbital wave functions and energies using a Dirac-Fock program [22]. The target level energies are just the ionization energy of the target plus the Coulomb energy of the target electron in the projectile potential, less the energy of the electron in the target potential; the internuclear Coulomb energy is ignored. The plotted radial interactions between the target and projectile states are qualitative.

To estimate the relative sizes of the rotational and radial couplings we calculated the reduced matrix elements $[\mathbf{L}_y]_{ij}$ and $[\partial/\partial R]_{ij}$. The reduced rotational matrix element can be written as $[\mathbf{L}_y]_{ij} = \mathbf{A}_{ik}^\dagger [\mathbf{L}_y^{\text{AO}}]_{kn} \mathbf{A}_{nj}$ and the radial coupling elements can be written as

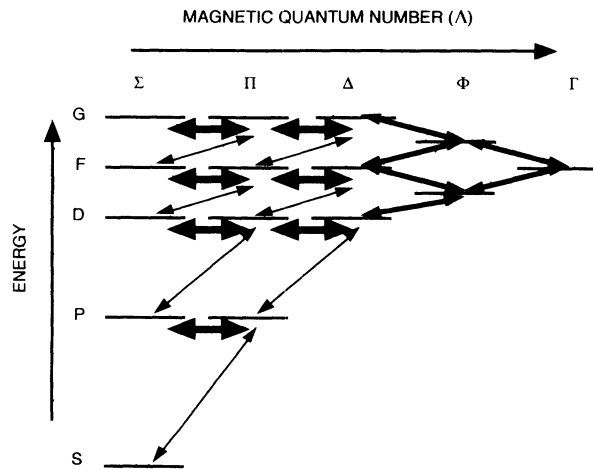


FIG. 6. Schematic diagram of rotational coupling near the crossing radius in the system $(\text{ArNa})^{8+}$. The weight of each arrow indicates the strength of the coupling. This diagram is also quantitatively accurate for the system $(\text{NeNa})^{8+}$ past about 100 a.u., where the 9P levels leave the Stark manifold.

$[\partial/\partial R]_{ij} = \mathbf{A}_{ik}^\dagger (\partial/\partial R) \mathbf{A}_{kj}$, where $[\mathbf{L}_y^{\text{AO}}]_{nk} \equiv \langle \Phi_n^0 | \mathbf{L}_y | \Phi_k^0 \rangle$ is the rotational coupling matrix element between projectile atomic orbitals states $|\Phi_i^0\rangle$ and $\mathbf{A}_{ij} \equiv \langle \Phi_i^0 | \Phi_j \rangle$ is the overlap matrix between the atomic and molecular orbitals. Overlap between projectile and target orbitals was ignored; these are negligible at distances much greater than the crossing radius, but are significant near the crossing radius.

Explicitly, the rotational coupling between atomic orbitals is

$$[\mathbf{L}_y^{\text{AO}}]_{nk} \equiv \langle \Phi_n^{\text{AO}} | \mathbf{L}_y | \Phi_k^{\text{AO}} \rangle = R_{nk} \langle Y_{lm(n)} | \mathbf{L}_y | Y_{lm(k)} \rangle, \quad (6)$$

where

$$|\Phi_n^{\text{AO}}\rangle = R_{nl}(r) Y_{lm(k)}(\theta, \phi),$$

$$R_{nk} \equiv \int R_n(r) R_k(r) r^2 dr.$$

From Bethe and Salpeter [23]

$$(\mathbf{L}_x \pm i \mathbf{L}_y) Y_{lm} = -\sqrt{(l \mp m)(l \pm m + 1)} Y_{l, m \pm 1}, \quad (7)$$

so

$$\langle Y_{lm+1} | \mathbf{L}_y | Y_{lm} \rangle = i \sqrt{(l-m)(l+m+1)}, \quad (8a)$$

$$\langle Y_{lm-1} | \mathbf{L}_y | Y_{lm} \rangle = -i \sqrt{(l+m)(l-m+1)}, \quad (8b)$$

or

$$[\mathbf{L}_y^{\text{AO}}]_{ij} = i R_{ij} \delta_{l_i, l_j} [(\sqrt{(l_i - m_i)(l_i + m_i + 1)} \times \delta_{m_i, m_j+1} - \sqrt{(l_i + m_i)(l_i - m_i + 1)} \times \delta_{m_i, m_j-1})]. \quad (9)$$

E. Qualitative results of matrix element calculations

We calculated the matrix elements between the states of the collision systems and evaluated the strength of each transition mechanism, which we defined as the root sum square of the matrix element between each level and the adjacent levels. This parameter does not include the effects of energy splitting or velocity; however, the purpose of this calculation was to qualitatively estimate the strengths of each transition mechanism. Energy differences will suppress transitions to all but adjacent levels, and increased velocity should increase the strength of all transitions, especially those of large energy differences.

The behavior of “resolved” states (molecular states that are nearly pure atomic states), is significantly different than the behavior of “manifold” states (those that are strongly coupled to several other states and collectively form a structure similar to a Stark manifold). Ions with complex cores have more resolved states than ions with simple cores; in any ion the lower- L states become progressively more resolved with increasing internuclear radius (Figs. 1–3).

The qualitative results are summarized in Table I.

TABLE I. Qualitative comparison of secondary coupling mechanisms in resolved and manifold states.

	Radial coupling	Rotational coupling	
		Intersubshell	Intrasubshell
O^{8+} (hydrogenic ion ¹)	Negligible within 200 a.u. radius Falls off at R^{-1}	Falls off as R^{-2}	Same size as intersubshell rotational coupling
Ne^{8+} , Ar^{8+} (Non-hydrogenic ions)			
Resolved states	Falls off as R^{-4}	Falls off as R^{-4} Same size as radial coupling	Dominant coupling Falls off as R^{-2}
Manifold states	Dominant coupling Falls off as R^{-2}	Falls off as R^{-2}	Falls off as R^{-2} Smaller in simple ions than complex ions

F. Qualitative description of a collision

The dynamics of one-electron (hydrogenic) systems are well understood, and so we discuss such a system as a basis for an understanding of electron capture, with an emphasis on the importance of secondary interactions; we will then discuss how adding core electrons to both the target and the core affect capture processes. In the hydrogenic system $(OH)^{8+}$ (Fig. 1) the exit channels form a Stark manifold, atomic hydrogen states perturbed by the electric field of the target ion. As the internuclear radius approaches infinity, the eigenstates approach hydrogenic parabolic wave functions, which can then be decomposed into spherical NLM wave functions. The entrance channel $\Sigma 3S_H$ interacts radially with the $\Sigma 9S_O$ state at the crossing radius of 18 a.u. The remaining $\Sigma 9O$ states have a different symmetry unique to one-electron molecules [21] and so do not interact radially with either the $\Sigma 3S_H$ or the $\Sigma 9S_O$ states. The $\Sigma 9S_O$ state couples rotationally to the $\Pi 9P_O$ state (secondary postcapture interactions, Fig. 4), which in turn is coupled to the $\Sigma 9P_O$ and $\Delta 9D_O$ states, and the wave function is thus distributed among the various eigenstates. The final L and M distribution of the projectile is determined by the distribution of the final state of the projectile among the Stark wave functions, which is determined by the secondary rotational couplings; hence, the final L and M distributions are determined by these interactions. Most calculations and experiments show that at intermediate velocities ($v \approx 0.5-1.0$ a.u.), the L distributions are approximately statistical; this is consistent with equal population in each M state and therefore a polarization of zero. Radial interactions between projectile orbitals is negligible far from the crossing radius.

Increasing the complexity of the core by adding both nuclear charge and core electrons (Figs. 2 and 3) increases the fine-structure splitting of the exit channels, reduces coupling between resolved levels, and increases radial couplings between the entrance channel and the high- L exit channels. As each level becomes resolved

from the Stark manifold, rotational and radial coupling between the resolved level and other subshells weakens, and rotational coupling to other Λ states of the level's subshell strengthens. These effects are combinations of the increase in the oscillation frequency of the complex exponential in Eq. (4) and in a decrease in the size of the reduced matrix elements $[L_y]_{ij}$ and $[\partial/\partial R]_{ij}$. Because of the weakening of the intersubshell couplings, the final L distributions of ions with complex cores (particularly at low velocity) are more representative of the primary capture process than for hydrogenic systems. However, as velocity increases both the radial and rotational couplings strengthen and the importance of potential interactions decreases, so the effect of the core on both polarization and cross-section measurements should decrease.

III. EXPERIMENTAL PROCEDURE

The Stanford Recoil Ion Source (SRIS), the apparatus used to produce the recoil ion beam, has been described elsewhere [24,25]. The SRIS is capable of producing a typical current of 200 pA of Ne^{8+} or Ar^{8+} with a beam energy of 4000 eV; the maximum current measured is 1000 pA. The recoil beam is chopped at about 17 Hz to allow background subtraction in a digital lock-in mode, is passed through an atomic sodium beam at the interaction region, and then dumped into a Faraday cup where the current is collected and integrated. Light emitted from the interaction region is passed through a fused silica vacuum window and collected by a fused silica lens, is directed by a front surface mirror into the entrance slits of a 640 mm spectrometer, and is detected by a photon-counting photomultiplier tube placed at the exit port of the spectrometer. A modification of the program MASTER [26] is run on an IBM-AT to acquire and analyze data from the PMT and Faraday cup. We used narrow entrance slits and a position sensitive PMT to locate and identify the fine-structure lines of the spectra, and wide slits and a nonimaging PMT to measure the line intensities and polarizations as functions of velocity.

The solid angle subtended by the vacuum window as seen from the center of the integration region is 0.324 sr, which corresponds to an effective aperture of $f/1.6$. The lens position is chosen to produce an image at the slits with a magnification of 2.9 and an image aperture of $f/4.6$. The square grating has an aperture of $f/4.1$, so 64% of the light passing through the slits is collected by the grating.

The sodium oven nozzle parameters are such that for typical oven temperatures of $\sim 400^\circ\text{C}$ the beam flow is in the effusive regime [27], with an areal density of $N(2.74 \times 10^{-4}) \text{ cm}$, where N is the number volume density inside the oven. At 400°C , the areal density is $1.4 \times 10^{12} \text{ cm}^{-2}$.

A. Cross-section determination

For each observed line we measure the number of photons detected and the integrated recoil beam charge to determine the line intensity normalized to the recoil beam current:

$$I_0 = \frac{N_{\text{signal}} - N_{\text{background}}}{Q_{\text{recoil}}} \frac{Q_{\text{ion}}}{\epsilon_{\text{detector}} T_{\text{spec}}(\Pi) C(\Pi)}, \quad (10)$$

where N_{signal} is the total photon rate observed with the recoil beam on, $N_{\text{background}}$ is the photon rate observed with the beam off, Q_{recoil} is the integrated recoil beam charge, Q_{ion} is the charge per recoil ion, $\epsilon_{\text{detector}}$ is the efficiency of the detector, Π is the polarization of the light, $T_{\text{spec}}(\Pi)$ is the transmission of the spectrometer, and $C(\Pi)$ is the fraction of emitted photons that enter the input window of the optical system.

Both the T_{spec} and C are dependent on the polarization of the light: T_{spec} because of the polarization characteristics of the diffraction grating, and C because the σ field emits a greater fraction of light at $\pi/2$ radians from the axis of quantization than does the π field. In the Appendix we derive the form of the product $T_{\text{spec}} C$.

The cross section for capture into the upper level of a spectral line is related to the normalized line intensity I_0 by

$$I_0 = \sigma_i \delta B_{ij}, \quad (11)$$

where σ_i is the cross section for capture into level i , δ is the areal target density (atoms/cm²), and B_{ij} is the branching ratio for optical decay of the upper level.

We determined the branching ratios by using the Dirac-Fock structure program AANC to calculate the wave functions of the active electron, and by calculating the dipole transition rates for optical decay for each level of interest. Since these are not autoionizing levels, the lifetime for each level i is given by $\tau_i = (\sum_{j,i} A_{ij})^{-1}$, where A_{ij} is the dipole transition rate to each lower level j . Therefore, the branching ratio for decay to a lower level j is given by $B_{ij} = A_{ij} \tau_i$. The calculated branching ratios are close to those of Lindgård and Nielsen [28].

The branching ratios for $\Delta L = -1$ transitions with $L_{\text{init}} \approx N_{\text{init}} - 1$ are close to 100%, so these are the brightest lines of the spectrum. These levels are nearly hydrogenic because high- L wave functions penetrate the core

very little, so the lines from transitions originating on the high- L levels (known as the Bohr levels) form an unresolved complex known as the Bohr line, which is typically 10–100 times as bright as any other line in the spectrum. The intensity of the Bohr line is a sum of the intensities of the high- L lines:

$$I_{\text{Bohr}} = \delta \sum_i \sigma_i B_i. \quad (12)$$

The cross sections determined from measurements of the intensity of the Bohr line are an average over the unresolved lines, weighted by branching ratio:

$$\sigma_{\text{Bohr}} \equiv \frac{I_{\text{Bohr}}}{\delta \sum_i B_i} = \frac{\sum_i B_i \sigma_i}{\sum_i B_i}. \quad (13)$$

The Bohr cross section quoted in the Results section of this paper is a weighted-average cross section per sub-shell; unless otherwise stated, for the Ne VIII spectrum the sum includes the $9L$, $9K$, and $9I$ levels, and for the Ar VIII spectrum it includes the $9L$ and $9K$ levels.

B. Polarizations and M_L population determination

The polarization of a manifold of lines $L \rightarrow L'$ is determined by the intensities I_σ and I_π of the σ and π radiation fields, as shown in the Appendix. In the SA limit the exit channels of the collision are described in an NLM atomic-orbital basis; however, each NLM orbital is spin coupled to a set of eigenstates of the Hamiltonian in the $NSLJM$ basis. If the spin-orbit-coupling precession rate is much faster than the electromagnetic decay rate of the eigenstates, then the final state of the projectile resolves into the eigenstates before decaying, and so the decay transition rates must be calculated in the spin-coupled basis. This condition is satisfied if the homogeneous widths of the eigenstates are narrower than the spin-orbit splitting between them; that is, if the states are well resolved. This is the case in all the states considered here.

In order to determine the polarization of a manifold of lines given the M_L distribution it is necessary to determine the density matrix in the $NSLJM$ basis from the density matrix in the M_L basis, and then determine the transition rates into the σ and π fields from the diagonal elements of the $NSLJM$ density matrix. Since the experiment is not sensitive to quantum beats we are not concerned with contributions from the off-diagonal elements of the $NSLJM$ density matrix. In Appendix B we present the procedure for calculating the σ and π field intensities given an M_L distribution.

The nature of the rotational and radial interactions allow some generalization of the M_L distribution. First, the rotational symmetry of the collision system dictates that the distribution be symmetric around $M_L = 0$. Next, the dominant primary capture process is a radial coupling that links only states of similar symmetry, which lead in the SA limit to states of identical values of $|M_L|$. Since the initial state of the Na atom is an $M_L = 0$ state

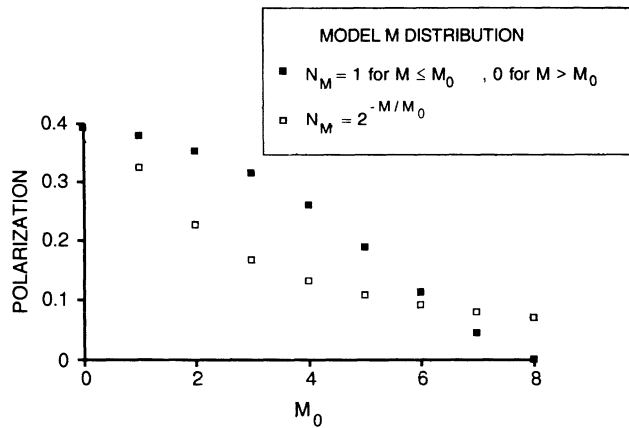


FIG. 7. Polarization of the 9-8 Bohr line as a function of the model parameter M_0 of the M_L distribution. Predictions are shown for two distributions: a step function (sharp cutoff model) and an exponential drop.

only $M_L=0$ states of the final ion would be populated in the absence of rotational coupling. Finally, since at low velocity the rotational interactions which populate states of higher $|M_L|$ are weak, the final distribution is dominated by low values of $|M_L|$.

In order to interpret the polarization data in terms of M_L populations we have calculated polarizations of light emitted at 90° from the axis of quantization for $L \rightarrow L-1$ transitions for singlet core ions, assuming complete mixing of the subshells $L=5$ to $L=8$ and two different M_L distributions which satisfy the above conditions:

$$N_M = \begin{cases} 1 & \text{when } |M_L| \leq M_0 \\ 0 & \text{otherwise} \end{cases}$$

and

$$N_M = 2^{-|M_L|/M_0}.$$

The second distribution is similar to the distribution calculated by Salin for hydrogenic systems [2]. The results as a function of the model parameter M_0 are presented in Fig. 7; clearly, quantitative interpretation of the polarization is dependent on the precise form of the M distribu-

TABLE II. Ne VIII spectral line wavelengths. X_n , unidentified line.

Transition	Predicted wavelength (nm)	Observed wavelength (nm)	Discrepancy pred.-obs. values
9G-8F	434.115	433.876±0.004	+0.239
9H-8G	434.150	434.103±0.004	+0.047
Bohr line	434.192	434.192 ^a	a
X_1		437.759±0.007	
X_2		438.114±0.007	
X_3		438.692±0.008	
9S _{1/2} -8P _{1/2}	453.891	453.864±0.006	+0.007
9S _{1/2} -8P _{3/2}	454.396	454.400±0.005	-0.004

^aWavelength reference line.

TABLE III. Ar VIII spectral line wavelengths.

Transition	Predicted wavelength (nm)	Observed wavelength (nm)	Discrepancy pred.-obs. values (nm)
9P-8S	315.794		
9D-8P	321.834		
9G-8F	431.208	431±1	0.2
9H _{9/2} -8G _{7/2}	434.031	unresolved	
9H _{11/2} -8G _{9/2}	434.054	433.718±0.005	0.336
9I _{11/2} -8H _{9/2}	434.148	unresolved	
9I _{13/2} -8H _{11/2}	434.163	434.088±0.005	0.075
Bohr line	434.192	434.192 ^a	a
9D _{5/2} -8F _{7/2}	466.791	unresolved	
9D _{3/2} -8F _{5/2}	466.898	466.131±0.5	0.767
9P _{3/2} -8D _{5/2}	534.098	532.690±0.008	1.408
9P _{1/2} -8D _{3/2}	535.971	534.534±0.015	1.437
9S _{1/2} -8P _{1/2}	449.787	448.429±0.009	1.358
9S _{1/2} -8P _{3/2}	452.068	450.633±0.005	1.435

^aWavelength reference line.

tion, but both distributions have the same qualitative trend: as M_0 increases, the polarization decreases. Since the nonzero M_L states are populated only through rotational coupling, the degree of anisotropy is often regarded as a measure of the strength of the rotational coupling. As we shall see, this is an oversimplification.

C. Resolution and slit width

The spectrometer is equipped with a variable 0–2 mm slit, and with a fixed 1-cm slit; the width of the image of the interaction region is 1 cm. Variations in the sodium oven density required that each sequence of measurements be performed within an hour, and so when making velocity-dependent measurements we used the 1-cm slit to allow rapid measurement of the line intensities. Given the spectrometer dispersion of 5 nm/cm, the resolution of the system with the 1-cm slit was 5 nm; velocity studies were therefore restricted to lines resolved from the Bohr line by at least 5 nm. Table II is a list of the lines of the Ne VIII spectrum that we were able to observe; of the fine-structure lines only the 9S-8P lines are sufficiently resolved from the Bohr line to allow a measurement of the velocity dependence. By narrowing the slits and making a 4-h exposure we were also able to measure the cross sections of the remaining weak fine-structure lines at a single velocity. Table III is a list of the observed Ar VIII lines; of these the 9S-8P, 9P-8D, and 9D-8F lines are sufficiently resolved to measure a velocity dependence.

IV. RESULTS AND DISCUSSION

A. Ne⁸⁺ + Na → Ne⁷⁺ + Na⁺

1. Line identification

Most of the observed lines of the Ne VIII spectrum were sufficiently close to predictions of the multiconfigurational Dirac-Fock code to allow unambi-

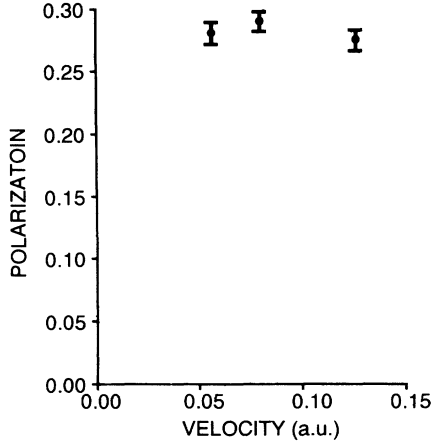


FIG. 8. Polarization of the $N=9-8$ Bohr line of Ne VIII as a function of projectile velocity.

guous assignment. However, the three lines marked X_n in Table II were not unambiguously assigned, but are close to the $9S-8P$ manifold of the metastable ($1s2s$) Ne VIII spectrum. Lembo [10] has measured the ratio of L to K x-ray intensities after capture to be three to one, but did not see any spectral line attributable to metastable cores and concluded that the cores were destroyed by mixing of $2S$ and $2P$ states during the collision. To confirm that the X_n lines are in the Ne VIII spectrum we performed several tests. We looked for them with Ar^{8+} , Ne^{7+} , and Ne^{9+} projectiles with the Na target, and with Ne^{8+} and Ar^{8+} without the Na target; the lines were present only with collisions between Ne^{8+} and Na. We therefore interpret these lines as $9S-8P$ transitions in metastable ions, providing evidence for the conservation of the core during the collision. We have not studied the polarization or velocity dependence of these lines.

2. Polarization measurements

In Fig. 8 we present the polarization of the Bohr lines of Ne VIII as a function of velocity; the polarization is in the range 0.25–0.30 and is independent of velocity. Comparing the results to Fig. 7, we see that if the final state of the electron were a pure σ state the polarization would be $\Pi=0.39$. The measured polarization is the same as that of the exponential distribution with a model half-width of $M_0=1$ to 1.5, and the sharp cutoff distribution with a model half-width of $M_0=3$ to 4. If the complete mixing hypothesis were valid for all the subshells, as would be true if the system were behaving like a hydrogenic system, then the M_L distribution would determine the population of each subshell. Calculating the population distribution with these two models, we would predict a ratio of the average population of the higher- L levels to the population of the S level of 2.5 for the exponential model and 7 for the sharp dropoff model.

3. Cross-section measurements

In Fig. 9 we present the measurements of σ_{9S} and σ_{Bohr} for Ne^{7+} as functions of velocity, along with our

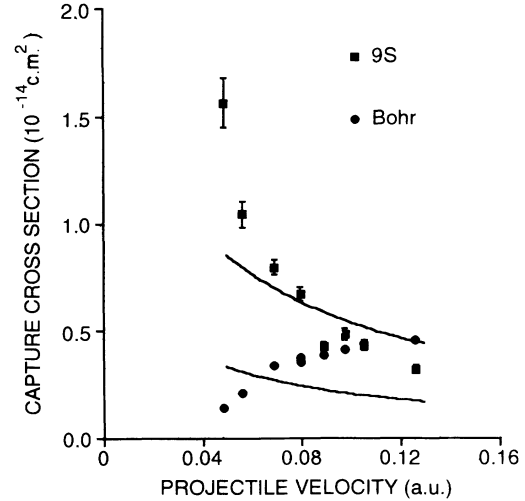


FIG. 9. Partial cross sections σ_{Bohr} and σ_{9S} for capture into Ne^{7+} as functions of projectile velocity. The Bohr cross section is a weighted average over the $9L$, $9K$, $9I$, $9H$, and $9G$ levels. The curves are MLZ theoretical predictions calculated using the matrix elements listed in Table IV.

MLZ predictions. The MLZ predictions were calculated using matrix elements described by Eq. (2), using the value of A given in Table IV; this value was chosen to provide the best fit to the $9S$ data at low velocities. We have taken secondary interactions into account by assuming complete mixing in the Stark manifold, so the Bohr value represents an average over all the levels except for the $9S$ level; excluding the $9P$ and $9D$ level would result in a much smaller prediction.

The S levels dominate the capture process for low velocities, and the Bohr levels at higher velocities. The low-velocity data disagree with Salin's complete mixing model, which predicts a value of σ_{Bohr} equal to or higher than σ_{9S} at all velocities, but is in qualitative agreement with the prediction of Harel and Jouin for capture by partially stripped ions [3]. At higher velocities the core interaction in the OEDM framework is reduced, and so the cross sections should resemble the hydrogenic cross sections, approximated by the complete mixing model. The ratio $\sigma_{Bohr}/\sigma_{9S}$ at high velocities is consistent with the value ~ 2.5 predicted by the complete mixing model with exponential dropoff and the polarization data.

We have searched for the $N=10-9$ Bohr line and found it to be negligibly weak; therefore, in calculating the capture cross sections we have neglected the effects of capture into the $N=10$ or higher levels, which would populate the $N=9$ level through cascade decays. Both the CBM model and the MLZ model with Taubjerg's matrix

TABLE IV. Values of the parameter A from Eq. (2) used to calculate MLZ cross sections.

System	A
$(NeNa)^{8+}$	12
$(ArNa)^{8+}$	5.5

elements predict negligible capture into the $N = 10$ level.

The uncertainties in our cross-section measurements are statistical; systematic errors due to uncertainties in target density may be on the order of a factor of 2.

4. Comparison of cross-section measurements with theoretical predictions

There have been no close-coupling calculations performed for this collision system. However, calculations of the classical barrier model and the absorbing sphere model are straightforward and results are presented in Table V. The observed total cross section is about a factor of 5 lower than that predicted by the classical barrier model; the remaining discrepancy may be due to a systematic error in calculating the density of the sodium target and due to capture into unobserved levels. The ASM predictions are two orders of magnitude too small.

We also compare the partial cross-section data to the MLZ model in Fig. 9. Since well-resolved levels have weaker intersubshell interactions we expect the MLZ model to fit data for these levels best; therefore we attempted to adjust Taubjerg's matrix elements to fit the S level data at low velocities. Our MLZ predictions fit the data best with matrix elements larger than Taubjerg's by a factor of 12. For any reasonable fit of the S data the predicted Bohr level cross section decreases with velocity.

If the Bohr levels were populated by primary interactions (a necessary condition for the validity of the L distribution predictions of the MLZ models) and the matrix elements between these levels and the incoming channel were smaller than the elements for lower- L levels, then at low velocities capture would be into the Bohr levels and the system would pass adiabatically through the S and P pseudocrossings and at high velocities the system would pass diabatically through the Bohr pseudocrossings and capture would be into the S and P levels. This is the reverse of the observed behavior.

5. Theoretical interpretation

In a hydrogenic system the primary capture is into the $L = 0$ (S) exit channel. The high- L levels are populated by rotational coupling from this channel. Unlike the hydrogenic system, the $(\text{NeNa})^{8+}$ system (Fig. 2) has core electrons in both the projectile and target. These cores break the symmetry of the one-electron system and introduce additional radial couplings between the entrance channel and the exit channels. The projectile core also breaks the degeneracy of the final states, and the $9S$ level

TABLE V. Comparison of theoretical and experimental values of σ_{tot} for Ne^{8+} and Ar^{8+} projectiles. σ_{tot} is a sum over observed lines (S, G, H, I, K, L at 0.089 a.u. for Ne^{8+} and S, P, D, F, I, K, L at 0.04 a.u. for Ar^{8+}) assuming that the cross sections of all levels in the unresolved Bohr complex are equal.

Projectile	Total $N = 9$ capture cross section (cm^2)		
	Observed	CBM	ASM
Ne^{8+}	$> 1.9 \times 10^{-14}$	1.0×10^{-13}	1.0×10^{-16}
Ar^{8+}	$> 3.3 \times 10^{-14}$	1.0×10^{-13}	10×10^{-16}

in particular is nearly fully resolved at the crossing radius. The separation of the $9S$ level from the Stark-like manifold reduces the overlap matrix $\mathbf{A}_{\Sigma 9S, \Pi 9P}$ and weakens the radial and rotational coupling between the $\Sigma 9S$ and $\Pi 9P$ levels (Fig. 5). If the primary-capture process is dominated by capture into the S level, then when the $\Sigma 9S$ - $\Pi 9P$ coupling is weak (as at low velocity) the final population is dominated by the $9S$ state. At higher velocity even the weakened couplings are strong enough to depopulate the S level. In the OEDM framework this effect appears as a relative weakening of the potential coupling, allowing the radial and rotational couplings to behave as in the hydrogenic system in which the S level is poorly populated.

The effect of the core for this system is less for the remaining rotational couplings than the $\Sigma 9S$ - $\Pi 9P$ coupling. Therefore, the M and L distributions of the higher- L levels should be similar to the hydrogenic case, and the polarization of the Bohr line should be similar to that of a hydrogenic $\text{O}^{8+} + X$ system. The measured polarization is consistent with that observed for the same system by Lembo *et al.* [11] and with the polarization calculated by Lembo from the M distribution calculated by Salin [2] for hydrogenic systems.

Comparisons of the MLZ model with the experimental data strongly imply that either secondary interactions (ignored by MLZ) significantly affect the partial cross sections, or the matrix elements we used were incorrect. In order to correspond with the experimental data the high- L pseudocrossing matrix elements would have to be much larger and the S matrix element smaller than our predictions.

B. $\text{Ar}^{8+} + \text{Na} \rightarrow \text{Ar}^{7+*} + \text{Na}^+$

1. Polarization measurements

In Fig. 10 we present the polarization of the Bohr line of Ar VIII as a function of projectile velocity. The polarization increases with increasing velocity, implying that the population of the low- M states is increasing relative to the population of the higher- M states. The polarization is also significantly lower than the polarization of the

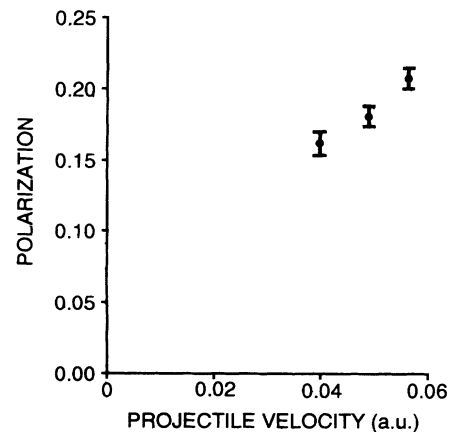


FIG. 10. Polarization of the $N = 9-8$ Bohr line of Ar VIII as a function of projectile velocity.

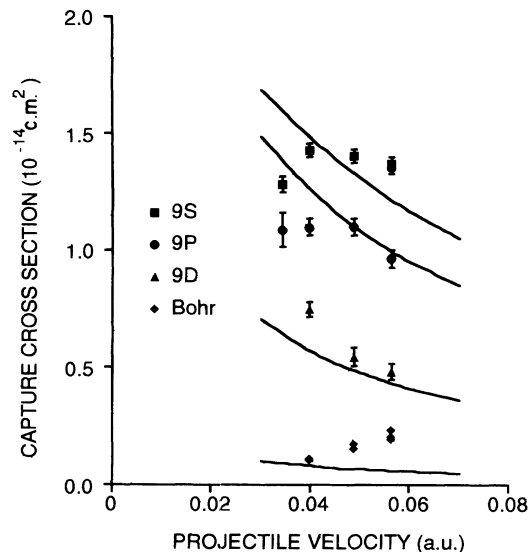


FIG. 11. Partial cross sections for capture into Ar^{7+*} as functions of projectile velocity. The Bohr cross section is a weighted average over the $9L$, $9K$, and $9I$ levels. The curves are MLZ theoretical predictions calculated using the matrix elements listed in Table IV.

Ne VIII Bohr line, implying a broader M distribution for the argon system due to the increased rotational coupling in the Stark-like manifold. As velocity increases the effect of the core on the polarization decreases, as predicted above. Not presented are measured polarizations for both the $9P$ - $8D$ and $9D$ - $8F$ lines. For both these lines the polarization is zero to within expected error.

2. Cross-section measurements

In Fig. 11 we present the measurements of σ_{9S} , σ_{9P} , σ_{9D} , and σ_{Bohr} for Ar^{7+*} as functions of velocity, again with MLZ predictions. The predicted Bohr cross section is a weighted average over all levels except $9S$, $9P$, $9D$, and $9F$. The low- L subshells dominate at all velocities used, in accord with Harel and Salin's prediction for low velocity. The L distribution at very low velocity, where both rotational and radial coupling are weak, should be representative of the primary-capture process; the data are consistent with this prediction and the observation that the radial coupling between the entrance channel and the exit channels should decrease with increasing L . As in the neon system, as the velocity increases the population distribution shifts toward the higher- L levels, reflecting the strengthening of rotational coupling with velocity.

3. Comparison of cross-section measurements with theoretical predictions

There have been no close-coupling calculations performed for this collision system. Results of CBM and ASM model calculations are presented in Table V. The observed cross sections are about a factor of 3 lower than the CBM cross sections and about two orders of magnitude higher than the ASM cross sections. Again, capture

into the unobserved levels would bring the observed total cross section close to the CBM cross section.

The partial cross sections of the low- L levels are fitted reasonably well by the MLZ predictions. Like the $(\text{NeNa})^{8+}$ system, the predicted Bohr cross sections drop with velocity while the experimental cross sections rise.

4. Theoretical interpretation

In the $(\text{ArNa})^{8+}$ system (Fig. 3) additional electrons in the core increase the resolution of the S level from the manifold and also resolve the P level and the D level partially. Radial interactions between the entrance channel and the higher- L levels may be stronger than in the $(\text{NeNa})^{8+}$ system. Evaluation of the rotational coupling matrix for this system shows that the resolved levels do not interact with levels of different subshells, and that the rotational coupling between the subshells in the Stark-like manifold is stronger than in the hydrogenic case (Fig. 6).

As mentioned before, the dominance of the low- L channels at low velocities is expected, given the assumption that the primary-capture process is dominated by capture into the $\Sigma 9S$ state and that at low-velocity rotational coupling is negligible. However, the low polarization of the Bohr line at low velocity implies much higher rotational coupling than for Ne^{8+} projectiles, and the velocity dependence of the polarization implies that rotational coupling is weakening with velocity. These data are most easily interpreted in terms of a model involving two mechanisms for populating the Bohr levels.

The first mechanism is the two-step process that populates the Bohr levels in hydrogenic systems and simple systems such as $(\text{NeNa})^{8+}$. The system passes diabatically through the Bohr level crossings and the electron is captured into the $9S$ level. As the projectile recedes, secondary interactions populate the Bohr levels. This mechanism would be characterized by the same high polarization of the $(\text{NeNa})^{8+}$ system. Since it requires diabatic passage through the Bohr level crossings, it dominates at high velocities.

The second mechanism is direct capture into the Bohr levels. Some of this capture will take place before the time of closest approach. During this time the rotational coupling is strongest and the high- Λ states of the manifold are easily populated. This mechanism would be characterized by poorly aligned states, and would dominate at low velocities when the system passes adiabatically through the high- L crossings.

The low polarization of the $9P$ - $8D$ and $9D$ - $8F$ lines is likely due to the fact that during the collision the rotational coupling between the $9P$ and $9D$ subshells and other subshells is not strong, whereas rotational coupling within the $9P$ and $9D$ subshells is strong. This coupling should quickly dealign these levels during the postcollision interactions.

C. Comparison of cross-section measurements to MLZ predictions

In both systems the MLZ model predicted cross sections much lower than the observed cross sections unless

we used matrix elements 5–12 times larger than Taubjerg's matrix elements. The low- L partial cross sections dominated the capture cross section at low velocities and decreased with increasing velocity, in qualitative agreement with the MLZ model. The high- L cross sections increased with increasing velocity, in qualitative disagreement with the model, implying either that these levels are populated primarily through secondary interactions, or that the matrix elements used for these pseudo-crossings were orders of magnitude too small.

These results are consistent with the theoretical interpretation we have proposed. Secondary interactions are ignored by the MLZ model; if the Bohr levels are populated primarily through radial interactions with low- L levels, then the MLZ model will underpredict the cross sections of these levels. This underprediction will worsen at higher velocities as the radial interaction strengthens. Given accurate matrix elements the model still should predict cross sections accurately for levels more strongly coupled to the entrance channel than to other exit channels; this seems to be the case for the (ArNa)⁸⁺ low- L levels.

V. SUMMARY

The lower limits on total capture cross sections for both the neon and argon systems are a factor of 100 greater than those predicted by Salop and Olson's absorbing sphere model, and are about a factor of 3–5 smaller than those predicted by the classical barrier model. The discrepancy with the CBM model may be partly due to capture into unobserved levels and systematic uncertainty in the target density and system detective efficiency. Using the multichannel Landau-Zener theory with matrix elements 5–12 times larger than Taubjerg's modification of Salop and Olson's matrix elements qualitatively describes the measured partial cross sections at low velocity, but the disagreement between prediction and experiment worsens at higher velocities.

The behavior of both systems as velocity increases approaches the predictions of Salin for a similar hydrogenic system [2]. This is consistent with the prediction of Harel and Salin [4] that core interactions should be less important at higher velocity. The systems showed high degrees of alignment at the highest velocity studied ($v \approx 0.13$ a.u.).

While the polarization of the Ne VIII Bohr line is independent of velocity in the range studied (0.05–0.13 a.u.), the polarization of the Ar VIII Bohr line increases with velocity, and is always lower than the hydrogenic prediction. The velocity dependence of the Ar VIII Bohr line polarization may be explained by a double population model, in which, at low velocity, direct capture from the entrance channel to the high- L levels dominates and rotational coupling during closest approach populates high- Λ states to produce low polarization light, and at high velocity, the dominant population mechanism is secondary capture from the lower- L levels after the collision, when rotational coupling is not strong and the high- Λ levels are not well populated.

ACKNOWLEDGMENTS

The authors would like to thank Professor Walter Meyerhof for his support of this work. This work was funded by the National Science Foundation, Grant No. PHY-86-14650.

APPENDIX A: THE LIGHT COLLECTION EFFICIENCY $C(\Pi)$

The light collection efficiency of the optical system is dependent on the polarization. This is because $\Delta m = 0$ transitions emit light in a σ field with intensity

$$I_{\sigma} = I_{\sigma}^0 \frac{3}{8\pi} \cos^2 \theta ,$$

where I_{σ}^0 is the intensity emitted into 4π sr, and θ is the angle from the axis of quantization to the direction of observation, and $\Delta m = \pm 1$ transitions emit light into a π field with intensity

$$I_{\pi} = I_{\pi}^0 \frac{3}{16\pi} (1 + \sin^2 \theta) .$$

For a given 4π intensity a σ field emits twice as strongly into a direction normal to the axis of quantization as a π field. The σ field is polarized entirely parallel to the axis of quantization, and the π field is generally polarized elliptically, and has polarization components both parallel and perpendicular to the axis of quantization. At $\pi/2$ radians from the axis the π field has no parallel polarization component. Over the finite solid angle of collection of our apparatus the parallel component of the π field is about 0.5% of the perpendicular component; we will ignore this component and assume that the π field is linearly polarized, and so the intensity of each polarization component incident on the spectrometer is

$$I_{\perp} = I_{\pi}^0 R_{\pi} \quad \text{and} \quad I_{\parallel} = I_{\sigma}^0 R_{\sigma\parallel} ,$$

where one can determine the values of R_{π} and $R_{\sigma\parallel}$ by integrating the π and σ flux densities over the solid angle of the vacuum window:

$$R_{\sigma} = \frac{1}{8} [4 - 3\cos(\Theta) - \cos^3(\Theta)] = 0.03337 ,$$

$$R_{\pi} = \frac{3}{8} [1 - \cos(\Theta)] = 0.01707 ,$$

where $\Theta = 0.3029$ radians is the half-angle of the window.

Both intensity and polarization measurements are complicated by the fact that the transmission of the spectrometer is polarization dependent. The intensity of light transmitted to the exit port of the spectrometer is

$$I_{\text{trans}} = I_{\perp} T_{\perp} + I_{\parallel} T_{\parallel} ,$$

where T_{\perp} , T_{\parallel} are the transmissions of the \perp and \parallel polarization components. Our apparatus is designed so light polarized parallel to the ion velocity (\parallel polarization) is incident on the grating with polarization parallel to the grating lines.

If there are no polarizing elements between the source and the spectrometer, then the intensities calculated above may be used for the incident intensities, and the transmitted intensity is then

$$I_{\text{trans}} = I_{\sigma}^0 R_{\sigma} T_{\parallel} + I_{\pi}^0 R_{\pi} T_{\perp}.$$

The absolute transmissions T_{\parallel} and T_{\perp} are not easily measurable, but the ratio $R_t \equiv T_{\perp}/T_{\parallel}$ is. The total emitted intensity, $I^0 = I_{\sigma}^0 + I_{\pi}^0$, is then calculable:

$$I^0 = I_{\text{trans}} \frac{1+R_t}{2T_n} \frac{1}{1+R_m} \left[\frac{1}{R_t R_{\sigma\perp}} + \frac{R_m}{R_{\pi}} \right],$$

where $R_m \equiv I_{\parallel}^m/I_{\perp}^m$ is the ratio of the measured intensities of the polarization components, $T_n \equiv \frac{1}{2}(T_{\parallel} + T_{\perp})$ is the transmission of unpolarized light.

To determine T_n we used the transmission curve provided by the manufacturer of the grating, and assumed that the only other restriction on transmission was the slight mismatch between the f /numbers of the image and the spectrometer. The ratio R_m is determined by inserting the polarization filter and measuring the intensity of each polarization component, and is closely related to the polarization of the emitted light

$$\Pi \equiv \frac{I_{\parallel} - I_{\perp}}{I_{\parallel} + I_{\perp}} = \frac{R_m R_t - 1}{R_m R_t + 1}.$$

Although it is possible, in principle, to determine the total emitted intensity I_0 when the polarization measurement is made, in practice this is not done because the polarizing filter reduces the signal size by a factor of 3; for statistics limited measurements, this increases the run time needed to achieve a given signal-to-noise ratio by a factor of 9. Therefore, for each cross-section determination we performed two experiments: one with the polarizing filter in place to determine the intensity ratio R_m (which also allows determination of the polarization), and one without the filter to measure the intensity I_{trans} . Finally, we determined the ratio R_t by measuring R_m as a function of wavelength for an unpolarized source; for $\Pi=0$, $R_t R_m = 1$.

APPENDIX B: CALCULATION OF σ and π FIELD INTENSITIES FROM THE M_L DISTRIBUTION OF EXIT CHANNELS

Let us consider only states coupled to a given L manifold of the projectile, with an initial valence electron spin S_e and projectile core spin S_c , and assume that the electron and core spins are conserved during the collision. For ions that obey L - S coupling, after the collision the valence electron and core spins will couple to produce a total ion spin S ,

$$|S_c S_e M_c M_e\rangle = \sum_{S, M_S} |S_c S_e S M_S\rangle C(S_c S_e M_c M_e; S M_S),$$

where

$$C(S_c S_e M_c M_e; S M_S) \equiv \langle S_c S_e S M_S | S_c S_e M_c M_e \rangle$$

is the Clebsch-Gordan coefficient. If the final projectile wave function for a given trajectory is given by the sum

over exit channels,

$$|\Psi\rangle = \sum_{M_L} a_{M_L} |L M_L\rangle |S_e M_e\rangle |S_c M_c\rangle,$$

in the spin-orbit-coupled basis the final state is

$$|\Psi\rangle = \sum_{J, M_J} b_i |S L J M_J\rangle,$$

where

$$b_i = \sum_{M_L} a_{M_L} \langle S L J M_J | L S_e S_c M_L M_e M_c \rangle$$

and

$$\begin{aligned} \langle S L J M_J | L S_e S_c M_L M_e M_c \rangle \\ \equiv C(S L M_S M_L; J M_J) C(S_c S_e M_c M_e; S M_S). \end{aligned}$$

The intensity of radiation from transitions from a single state $|S L_i J_i M_{J_i}\rangle$ to a lower state $|S L_j J_j M_{J_j}\rangle$ is proportional to the diagonal element of the density matrix $\rho_{ii} = \langle b_i^* b_i \rangle$. This is determined by the amplitudes a_i of the exit channels

$$\begin{aligned} \langle b_i^* b_i \rangle &= \sum_{M_{L_n}, M_{L_m}} \langle a_{M_{L_n}}^* a_{M_{L_m}} \rangle \\ &\quad \times \langle S L_i J_i M_{J_i} | L S_e S_c M_{L_n} M_e M_c \rangle \\ &\quad \times \langle S L_j J_j M_{J_j} | L S_e S_c M_{L_m} M_e M_c \rangle. \end{aligned}$$

The rotational symmetry of the collision system ensures that the density matrix of the exit channels is diagonal in M_L , so the populations of the eigenstates are

$$N_i \equiv \langle b_i^* b_i \rangle = \sum_{M_L} \langle a_{M_L}^* a_{M_L} \rangle \langle S L J M_J | L S_e S_c M_L M_e M_c \rangle^2.$$

The intensities of the σ and π fields emitted in transitions from a manifold of upper states i and lower states j are given by the sums [29]

$$\begin{aligned} I_{\sigma} &= C \sum_{i,j} N_i S_{ij} \left[\begin{array}{ccc} J_j & 1 & J_i \\ -M_i & 0 & +M_i \end{array} \right]^2, \\ I_{\pi} &= C \sum_{i,j} N_i S_{ij} \left[\left[\begin{array}{ccc} J_j & 1 & J_i \\ -1-M_i & 1 & +M_i \end{array} \right]^2 \right. \\ &\quad \left. + \left[\begin{array}{ccc} J_j & 1 & J_i \\ 1-M_i & -1 & +M_i \end{array} \right]^2 \right], \end{aligned}$$

where N_i is the population of the upper eigenstate i , and S_{ij} is the line strength between upper level i and lower level j . The line strengths are given by the formula

$$S_{ij}^{1/2} = D_{\text{line}} \mathbf{P}_{N_i L_i S}^{N_j L_j S},$$

where $\mathbf{P}_{N_i L_i S}^{N_j L_j S}$ is the reduced dipole matrix element, and

$$D_{\text{line}} = (-1)^{L_j + S + J_i + 1} \sqrt{(2J_i + 1)(2J_j + 1)} \begin{Bmatrix} L_j & S & J_j \\ J_i & 1 & L_i \end{Bmatrix}.$$

*Present address: Lunar Radiation Corporation, Madison WI.

†Present address: Max-Planck-Institut für Quanten Optik, 8046 Garching, Germany.

- [1] R. K. Janev, *Phys. Scr.* **T3**, 208 (1982).
- [2] A. Salin, *J. Phys. (Paris)* **45**, 671 (1984).
- [3] C. Harel and H. Jouin, *Nucl. Instrum. Methods Phys. Res. Sect. B* **23**, 98 (1987).
- [4] C. Harel and A. Salin, in *Electronic and Atomic Collisions, Invited Papers of the XVth International Conference on Photon, Electron, and Atomic Collisions*, edited by H. B. Gilbody, W. R. Newell, F. H. Read, and A. C. H. Smith (North-Holland, Amsterdam, 1988), p. 631.
- [5] C. L. Cocke, J. P. Giese, L. N. Tunnell, W. Waggoner, and S. L. Varghese, in *Electronic and Atomic Collisions, Invited Papers of the XVth International Conference on Photon, Electron, and Atomic Collisions*, edited by D. C. Lorents, W. E. Meyerhof, and J. R. Peterson (North-Holland, Amsterdam, 1986), p. 453.
- [6] D. Dijkkamp, D. Ćirić, and F. J. deHeer, in *Electronic and Atomic Collisions, Invited Papers of the XVth International Conference on Photon, Electron, and Atomic Collisions*, edited by D. C. Lorents, W. E. Meyerhof, and J. R. Peterson (North-Holland, Amsterdam, 1986), p. 445.
- [7] R. Geller and B. Jacquot, *Phys. Scr.* **T3**, 19 (1983).
- [8] E. D. Donets, *Phys. Scr.* **T3**, 11 (1983).
- [9] C. L. Cocke, *Phys. Rev. A* **20**, 749 (1979).
- [10] L. J. Lembo, Doctoral dissertation, Stanford University, 1987 (unpublished).
- [11] L. J. Lembo, K. Danzmann, Ch. Stoller, W. E. Meyerhof, and T. W. Hänsch, *Phys. Rev. A* **37**, 1141 (1988).
- [12] N. Bohr and J. Lindhard, *K. Dan. Vidensk. Selsk. Mat.-Fys. Medd.* **28**, (1954).
- [13] Knud Taulbjerg, *J. Phys. B* **21**, L367 (1986).
- [14] G. Herzberg, *Molecular Spectra and Molecular Structure*, 2nd ed. (Van Nostand, Princeton, NJ, 1950), Vol. 1, Sec. VI 3, p. 325.
- [15] N. Bohr and J. Lindhard, *K. Dan. Vidensk. Selsk. Mat.-Fys. Medd.* **28** (1954).
- [16] D. Dijkkamp, D. Ćirić, E. Vlieg, A. de Boer, and F. J. de Heer, *J. Phys. B* **18**, 4763 (1985).
- [17] R. E. Olson and A. Salop, *Phys. Rev. A* **14**, 579 (1976).
- [18] J. P. Hansen and K. Taulbjerg, *J. Phys. B* **21**, 2459 (1988).
- [19] M. Kimura, T. Iwai, Y. Kaneko, N. Kobayashi, A. Matsumoto, S. Ohtani, K. Okuno, S. Takagi, H. Tawara, and S. Tsurubuchi, *J. Phys. Soc. Jpn.* **53**, 2224 (1984).
- [20] B. H. Bransden, *Adv. At. Mol. Phys.* **15**, 263 (1979).
- [21] B. Judd, *Angular Momentum Theory for Diatomic Molecules* (Academic, New York, 1975).
- [22] I. P. Grant, B. J. McKenzie, P. H. Norrington, D. F. Mayers, and N. C. Pyper, *Comput. Phys. Commun.* **21**, 207 (1980).
- [23] Bethe and Salpeter, *Quantum Mechanics of One- and Two-Electron Atoms* (Plenum, New York, 1977), p. 7.
- [24] L. J. Lembo, K. Danzmann, Ch. Stoller, W. E. Meyerhof, and T. W. Hänsch, *Phys. Rev. Lett.* **55**, 1874 (1985).
- [25] L. J. Lembo, Ch. Stoller, K. Danzmann, W. E. Meyerhof, T. W. Hänsch, and R. Gerson, *Nucl. Instrum. Methods Phys. Res. Sect. B* **23**, 101 (1987).
- [26] Michael Prior (private communication).
- [27] L. Vályi, *Atom and Ion Sources* (Wiley, London, 1977).
- [28] Anders Lindgård and Svend Erik Nielsen, *At. Data Nucl. Data. Tables* **19**, 533 (1977).
- [29] R. Cowan, *The Theory of Atomic Structure and Spectra* (University of California Press, Berkeley, 1981).